International Conference on Space Optics—ICSO 2018

Chania, Greece

9–12 October 2018

Edited by Zoran Sodnik, Nikos Karafolas, and Bruno Cugny

Electro-optical performance of the Ingenio/SEOSAT primary payload

C. Miravet

G. Taubmann

G. Santos

D. Zorita

et al.

International Conference on Space Optics — ICSO 2018, edited by Zoran Sodnik, Nikos Karafolas, Bruno Cugny, Proc. of SPIE Vol. 11180, 111806W · © 2018 ESA and CNES · CCC code: 0277-786X/18/$18 · doi: 10.1117/12.2536167

Electro-optical performance of the Ingenio/SEOSAT primary payload

C. Miravet *[a], G. Taubmann[a], G.Santos[a], D. Zorita[a], I. Cabeza[b], A. Marini[c], F. Reina[c], A. Popescu[c]

[a]SENER Ingeniería y Sistemas, C\Severo Ochoa 4, PTM, Tres Cantos, 28760 Madrid, Spain;
[b]AIRBUS Defence and Space, Avda. de Aragón 404, 28022 Madrid, Spain;
[c]ESTEC-ESA, postbus 299, Keplerlaan 1, 2200 AG Noordwijk, The Netherlands

ABSTRACT

Ingenio/SEOSAT is a high-spatial-resolution optical mission developed under the Spanish Earth Observation National Program for Satellites (PNOTS), and managed technically in the framework of an ESA contract. It features as Primary Payload (PP) a high-resolution optical payload with one 2.5 meter resolution panchromatic channel and four 10 meter resolution visible/near infrared spectral channels. It is based on a twin Korsch telescope concept, each telescope covering half of the instrument's swath width. At the present stage, the principal payload has undergone the vibration and environmental tests, and the final performance test campaign has been completed successfully. In this communication, we will present the main measured optical performance parameters, and its relation to predictions obtained from the different computer models. First, the payload's geometric performance is addressed in the paper, with focus on parameters such as the spatial sampling angle, detection line angle and distortion. On a second group, wavefront error and modulation transfer function are reviewed. Finally, radiometric performance is considered, with parameters such as radiance saturation levels and signal-to-noise ratios at defined minimum and reference radiances. All instrument performances have been measured at Thales Alenia Space in Cannes with set-ups developed specifically by Thales Alenia Space for Ingenio/SEOSAT (i.e. Modulation Transfer function, straylight and radiometric measurements).

Keywords: Ingenio/SEOSAT, Korsch telescope, geometric performance, MTF, image quality, radiometric performance

1. INTRODUCTION

Ingenio/SEOSAT is a high-spatial-resolution optical mission developed under the Spanish Earth Observation National Program for Satellites (PNOTS), and managed technically in the framework of an ESA contract. It features as Primary Payload (PP) a high-resolution optical payload with one 2.5 meter resolution panchromatic channel and four 10 meter resolution visible/near infrared spectral channels. It is based on a twin Korsch telescope concept, each telescope covering half of the instrument's swath width. In this communication, we will present the main measured optical performance parameters, and its relation to predictions obtained from the different computer models.

In section 2 is presented a brief description of the Ingenio/SEOSAT primary payload, including focal plane architecture. In section 3 is detailed the measured geometric performance, including spatial sampling angle, detection line angle and distortion, and their relation to the optical model predictions. In section 4 is presented the wavefront error measurements along the field of view of the panchromatic channel of both cameras, and its relation to the predictions obtained from the performed tolerancing analysis. In section 5 are presented the measured modulation transfer function (MTF) values at Nyquist frequency, for the panchromatic and multi–spectral channels of both cameras, together with the estimated values at end-of-life conditions. Finally, in section 6 is addressed radiometric performance, through parameters such as radiance saturation levels and signal-to-noise ratios at defined reference and minimum top-of-atmosphere radiances.

*carlos.miravet@sener.es; www.ingenieriayconstruccion.sener

2. INGENIO/SEOSAT PRIMARY PAYLOAD

Ingenio/SEOSAT[1-6] features a Primary Payload (PP) with one 2.5 meter resolution panchromatic (PAN) channel and four 10 meter resolution multi-spectral (MS) channels, located respectively in the blue (B), green (G), red (R), and near-infrared (NIR) spectral regions. The payload is equipped with two identical cameras, each covering half of the instrument's swath width of 55 Km. In figure 1 is displayed a CAD model view of the payload (left panel), together with an image of the actual flight model (central panel). In the right panel, it is shown an image of the payload covered with thermal blankets, acquired during the thermal test campaign at INTA facilities.

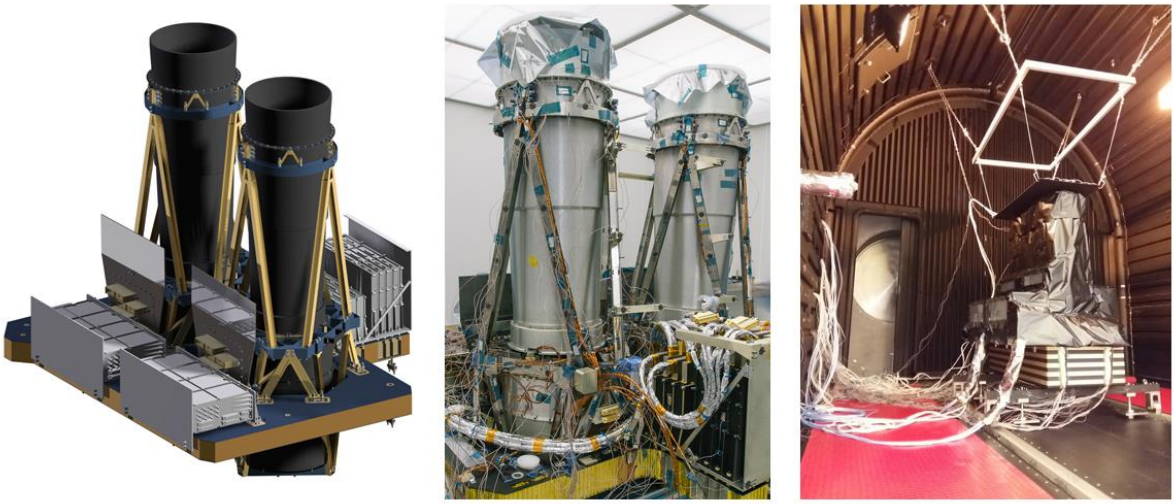

Figure 1. Ingenio/SEOSAT principal payload. Left: CAD model; center: flight model; right: flight model covered with thermal blankets, during the thermal test campaign.

The camera's optical subsystem is constituted by two identical all-reflective Korsch-type telescopes. In figure 2 (left panel) is presented the optical layout of the telescope. The system is composed of three conical on-axis mirrors plus a plane folding mirror, to redirect the image to the location of the focal plane (FP), in the upper part of the drawing. The telescope output is constituted by four image stripes, corresponding to the four slits cut on the primary mirror (at the center of the image), which act as field diaphragms of the telescope.

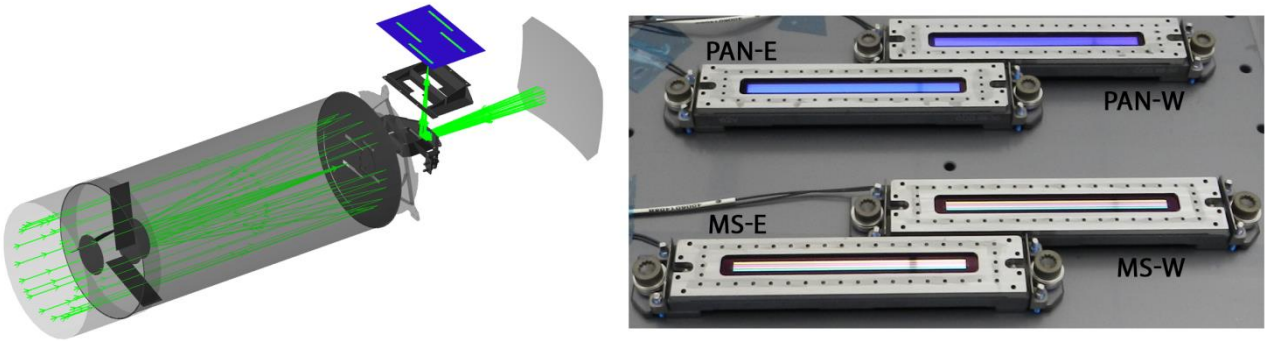

Figure 2. Left: Korsch telescope optical design; right: focal plane assembly, with two PAN and two MS detectors. 'E' and 'W' stand in the figure for east and west, respectively.

In the right panel of figure 2 is presented an image of the focal plane assembly. It is composed of two panchromatic (PAN) and two multi-spectral (MS) detectors, co-planarly located. Detectors on both channels are of CCD type. The detectors used for the PAN channel are based on the Time Delay and Integration (TDI) technology to increase the number of generated photo-electrons, with the corresponding increase in signal-to-noise ratio. A 4-line CCD detector has

been used to implement the MS channels, with each line devoted to sense one of the B, G, R and NIR bands. Each PAN and MS detector is mounted on its proper sub-assembly, which includes the filters defining the spectral bands and the corresponding proximity electronics.

3. GEOMETRIC PERFORMANCE

The PP geometric performance, and its relation to model predictions, have been evaluated from the acquired experimental data, which consists of the line-of-sight (LoS) direction cosines of 9 field points per detector, for a total of 72 LoS measurements in the PP. The LoS have been measured taking as reference a master optical cube in the payload. Before this data could be exploited, it has to be transformed to a reference frame linked to the properties of the optical design. Specifically, it has been computed the orientation of the reference frame that brings the measured data as close as possible to the design values, in a least squares error sense. This could be recognized as an instance of the Wahba's problem[7], well known in the star-tracker design field, which has been solved here by resorting to the standard SVD-based method. The procedure provides the transformation matrix from the master alignment cube to this PP optical reference frame, which has been used to express the measured direction cosines in a 'natural', optically meaningful frame.

In the left panel of figure 3 are displayed the obtained azimuth and elevation angles for the measured LoS points, in coordinates of the PP optical reference frame. The data corresponding to the PAN spectral channel appears at the bottom of the picture, depicted in black. The data for the MS detectors, measured on the green spectral channel, appears at the top of the picture. Positive and negative azimuth angles correspond to the first (T_1) and second (T_2) payload's cameras, respectively. The measured LoS points follow the spatial arrangement of detectors on the focal plane, with the effect of positive distortion bending slightly inwards the measured LoS points at the edge of each camera's field of view. Also, it can be noticed the slight 1 mrad elevation gap between both cameras. Measured LoS data have been used to fit polynomial models to azimuth and elevation angles as a function of pixel number, for each detector. These models have then been employed to evaluate fulfillment of PP geometric performance requirements. As an illustration, in the right panel of figure 3 are shown continuous models for elevation as a function of azimuth, obtained from the fitted polynomial models, and their relation to measured data, depicted as points in the figure. The displayed data encompasses all four detectors in the T_1 camera.

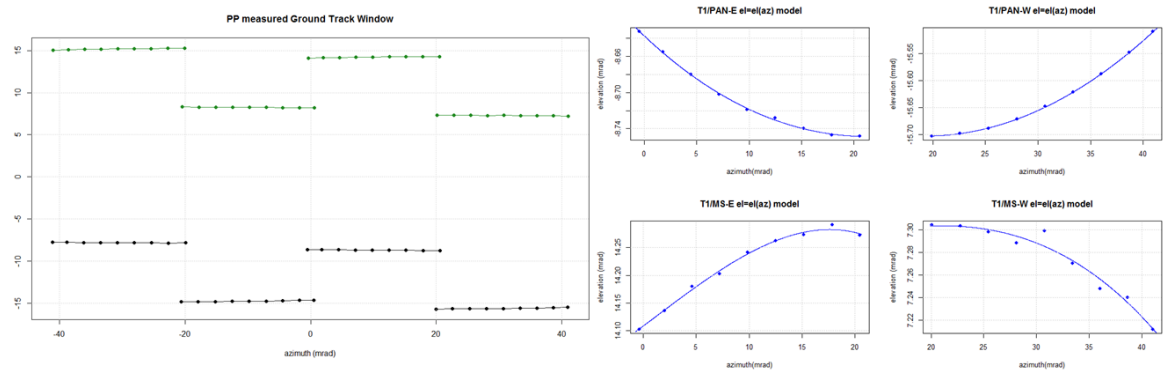

Figure 3. Left: performed line-of-sight measurements; right: derived elevation-azimuth continuous models

3.1 Spatial sampling angle (SSA)

In figure 4 is displayed the measured across-track SSA in the PAN channel, and its relation to model predictions. The displayed blue line has been obtained from measurements, by appropriate differentiation of polynomial models fitted to LoS measured data, as described in the previous section. The red solid line correspond to the model prediction for this parameter, with the red dashed lines marking the limits of a 1% interval around predicted values. As can be seen, the experimental values for both cameras lie with margin within the considered variation range, as imposed by the PP geometrical performance requirements. Also, the variation of the SSA along the instrument's field of view follows very closely the predicted values, anticipating an instrument's distortion close to nominal. Distortion is addressed in section 3.3.

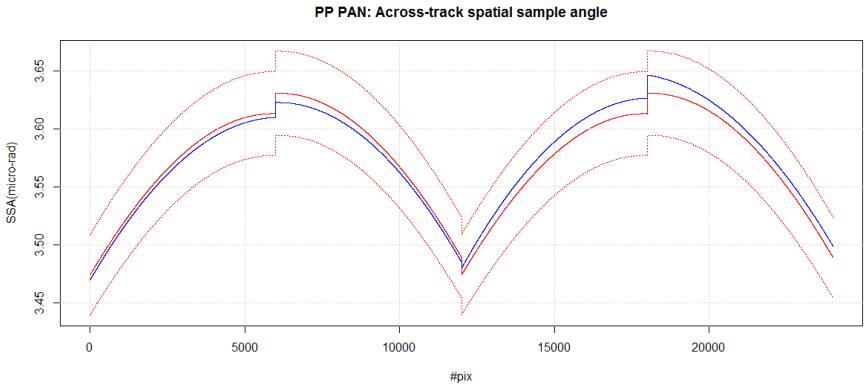

Figure 4. Model (red) and experimental (blue) across-track spatial sample angle curves for the PP's PAN spectral channel.

3.2 Detection line angle (DLA)

The detection line angle (DLA) is defined as the tilt of each detector with respect to each camera's optical axis. It has been determined here by solving the corresponding Wahba's problem between the LoS measurements for each detector, expressed in the corresponding camera optical reference frame, and the corresponding design values. The *x*-*y*-*z* Tait-Bryan angles for the resulting transformation have then been computed, with the sought DLA corresponding to the (roll) rotation angle along the *z* axis, oriented along the camera's optical axis.

In figure 5 are presented, for all four detectors in the T_1 camera, the LoS measurements (blue dots) and the continuous models derived from polynomial fittings (blue curve). The red dotted curves correspond to design values for that detector. Finally, red solid lines depict the model curves once transformed to the reference frame that provides the closest match to measured values, with excellent agreement between measurements and transformed model values.

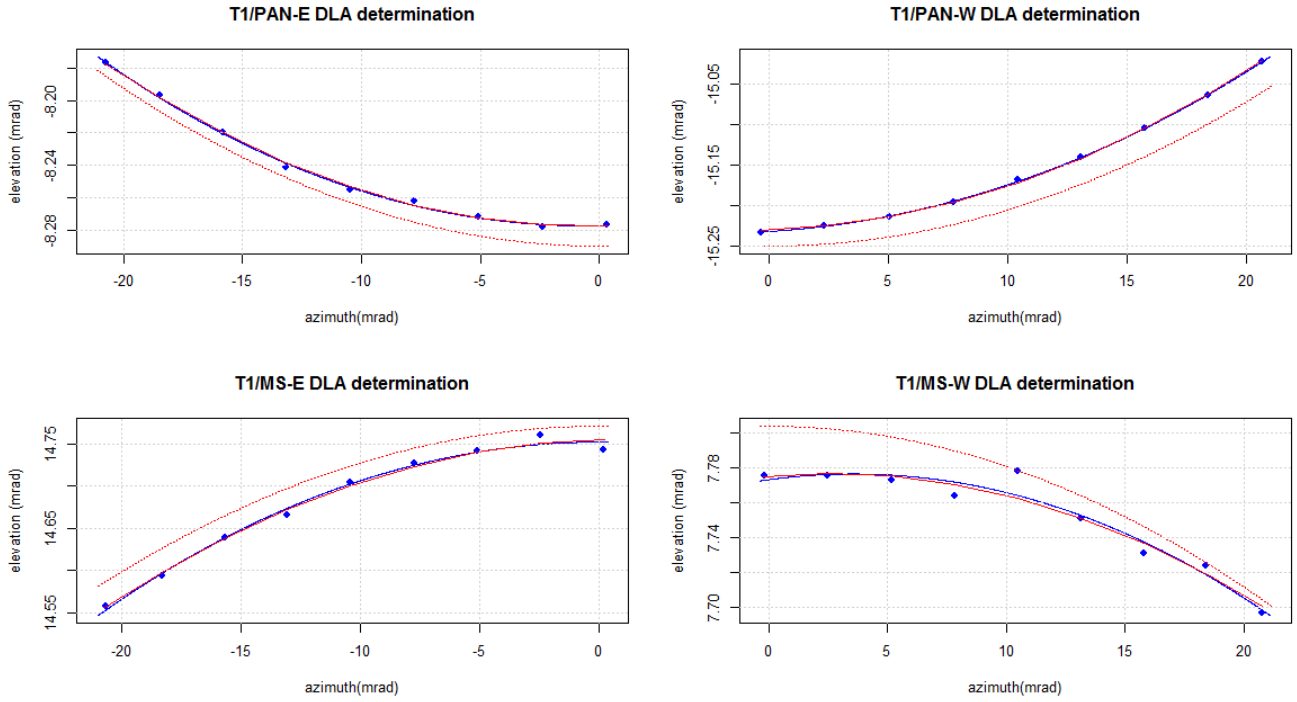

Figure 5. DLA determination for the four detectors in the T_1 camera.

In table 1 are presented the obtained DLA angles for the four detectors in each of the two PP cameras. The measured DLA angles are in all cases well below the maximum allowed value of 1 mrad. The accuracy of the implemented DLA evaluation method has been estimated through application of Efron's bootstrap method[8], a statistical probability density function estimation method. The estimated method's 3-σ accuracy values are 15 μrad for PAN detectors and 40 μrad for MS detectors, both below the accuracy requirement of 50 μrad.

Table 1. Measured detection line angles (DLA) for the eight PP detectors

Detector	T_1 camera	T_2 camera
PAN-E	3.8 μrad	1.1 μrad
PAN-W	15.6 μrad	6.1 μrad
MS-E	11.7 μrad	12.7 μrad
MS-W	21.0 μrad	30.6 μrad

3.3 Distortion

The geometric distortion error at a given pixel has been defined as the absolute value of the normalized difference between the theoretical and actual pixel angular coordinates. For azimuth, the theoretical angular coordinates have been fitted to a linear model. For elevation, a constant model has been used. In figure 6 is presented the comparison of measurements (blue) and model predictions (red) for the PAN channel. The left panel in the figure presents the results for azimuth distortion, whereas elevation distortion is presented in the right panel. The results in both cases are remarkably close to predictions, lying with margin below the 2% required limit. Results for the MS channel are similar to the ones presented for the PAN channel.

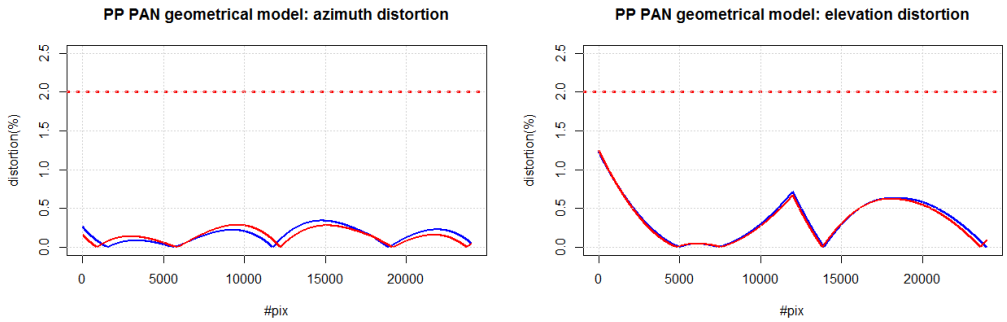

Figure 6. Model and measured distortion. Left: PAN azimuth distortion; right: PAN elevation distortion.

4. WAVEFRONT ERROR

The wavefront error (WFE) has been measured in each telescope at six field points in both the PAN (P_1-P_6) and MS-green (M_1-M_6) spectral channels. In figure 7 is presented a diagram showing the location of the measured points.

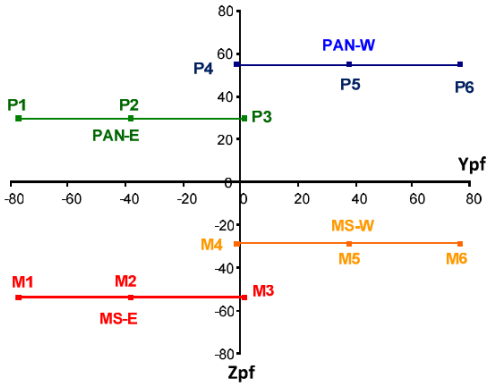

Figure 7. Location of the WFE measurement field points, in focal plane coordinates.

In table 2 are presented the compiled WFE RMS measurement results, together with the corresponding predictions obtained from a performed tolerancing analysis on the optical model, equipped with the measured WFE maps for the actual manufactured mirrors. Measurements are reported for the six measured field points of the PAN channel, the most critical one in terms of image quality. WFE units are in nm. Measurements and predictions are in excellent general agreement.

Table 2. Measured WFE for PAN channel of T_1 and T_2 telescopes, compared to tolerancing analysis predictions.

	P_1	P_2	P_3	P_4	P_5	P_6
T_1 WFE RMS measurements	**44**	**31**	**33**	**34**	**35**	**44**
T_1 WFE RMS predictions	40	33	34	37	41	50
T_2 WFE RMS measurements	**43**	**45**	**47**	**46**	**42**	**31**
T_2 WFE RMS predictions	44	36	31	35	42	38

5. MODULATION TRANSFER FUNCTION

The modulation transfer function (MTF) at Nyquist frequency has been measured in the PAN channel of each camera at the same six field points depicted in figure 7 for the WFE. In the MS spectral channels, with lower field-induced MTF variability, it has been measured in general at one field point per detector. In table 3 are presented the MTF values measured after PP integration, together with derived predictions for End-of-Life (EoL) conditions, once ground-to-orbit effects during the lifetime of the PP have been duly taken into account.

The list of quantified ground-to-orbit contributors encompasses both defocus and non-defocus related terms. Defocus terms include contributors such as gravity release and thermo-elastically induced defocus, effect of vibrations/launch and several long-term effects, such as those due to long-terms drifts in the temperature of the thermal refocus device on the secondary mirror, or radiation-induced changes in the curvature of the mirrors. Non-defocus related terms include gravity release and thermoelastic non-defocus effects, stray-light, TDI related effects (only in PAN) and some long term effects, as those induced by radiation on the CTI (charge transfer inneficiency) of the CCD detectors.

Table 3. Measured MTF for PAN and MS channels of T_1 and T_2 telescopes, and prediction at EoL conditions

MTF	P_1	P_2	P_3	P_4	P_5	P_6	B	G	R	NIR
T_1 ACT, measured	0,130	0,131	0,176	0,150	0,142	0,120	0,465	0,456	0,426	0,396
T_1 ACT, EoL prediction	**0,100**	**0,108**	**0,142**	**0,121**	**0,114**	**0,101**	**0,402**	**0,391**	**0,360**	**0,342**
T_1 ALT, measured	0,149	0,145	0,193	0,158	0,173	0,143	0,477	0,481	0,488	0,448
T_1 ALT, EoL prediction	**0,127**	**0,122**	**0,158**	**0,129**	**0,145**	**0,116**	**0,438**	**0,434**	**0,441**	**0,399**
T_2 ACT, measured	0,142	0,151	0,142	0,129	0,151	0,133	0,483	0,431	0,454	0,392
T_2 ACT, EoL prediction	**0,114**	**0,125**	**0,120**	**0,108**	**0,125**	**0,107**	**0,427**	**0,378**	**0,389**	**0,346**
T_2 ALT, measured	0,159	0,150	0,153	0,163	0,155	0,149	0,470	0,463	0,476	0,455
T_2 ALT, EoL prediction	**0,136**	**0,119**	**0,122**	**0,140**	**0,127**	**0,125**	**0,435**	**0,421**	**0,429**	**0,408**

For the PAN channel, predictions at the six measured field points are reported. For MS channels, predictions correspond to the M_3 field point. For each field point, two values are presented, corresponding to MTF values in the across-track (ACT) and along-track (ALT) directions. Predictions correspond exclusively to intrinsic PP parameters, and thus do not include the effect of satellite motion smearing, affecting primarily the MS MTF values on the ALT direction.

6. RADIOMETRIC PERFORMANCE

A radiometric set-up with an integrating sphere has been used to project a number (> 20) of uniform scenes with known radiances, covering the full dynamic range of PAN and MS channels in both cameras. At each radiometric scenario, a batch of 2,000 images were acquired from each detector in each camera, to enable accurate computation of average signal and signal standard deviation on a pixel-by-pixel basis. This data was then used to derive a number of radiometric performance parameters, such as radiance saturation levels, linearity assessment or signal-to-noise ratios (SNR). In figure 8 are presented the obtained radiance saturation values for the PAN and MS channels of the T_1 camera. Each

graph contains the values for a given spectral channel (PAN, blue, green, red and NIR). In each graph, the measured radiance saturation levels, projected to Beginning-of-Life (BoL) conditions, are depicted in blue. The horizontal dashed red lines correspond to the saturation radiance requirements at BoL conditions for that channel. In terms of saturation radiances, BoL rather than EoL conditions stand for the worst-case operational scenario during the lifetime of the PP.

In the PAN channel of this camera, as anticipated, saturation occurs at detector rather than at electronic level, with significant pixel-to-pixel level variations. The obtained values are in all cases above the threshold radiance value of 300 $Wm^{-2}sr^{-1}\mu m^{-1}$. In the MS channels, the reported saturation values meet or exceed the goal saturation values. Results for the T_2 camera are similar to the ones reported here.

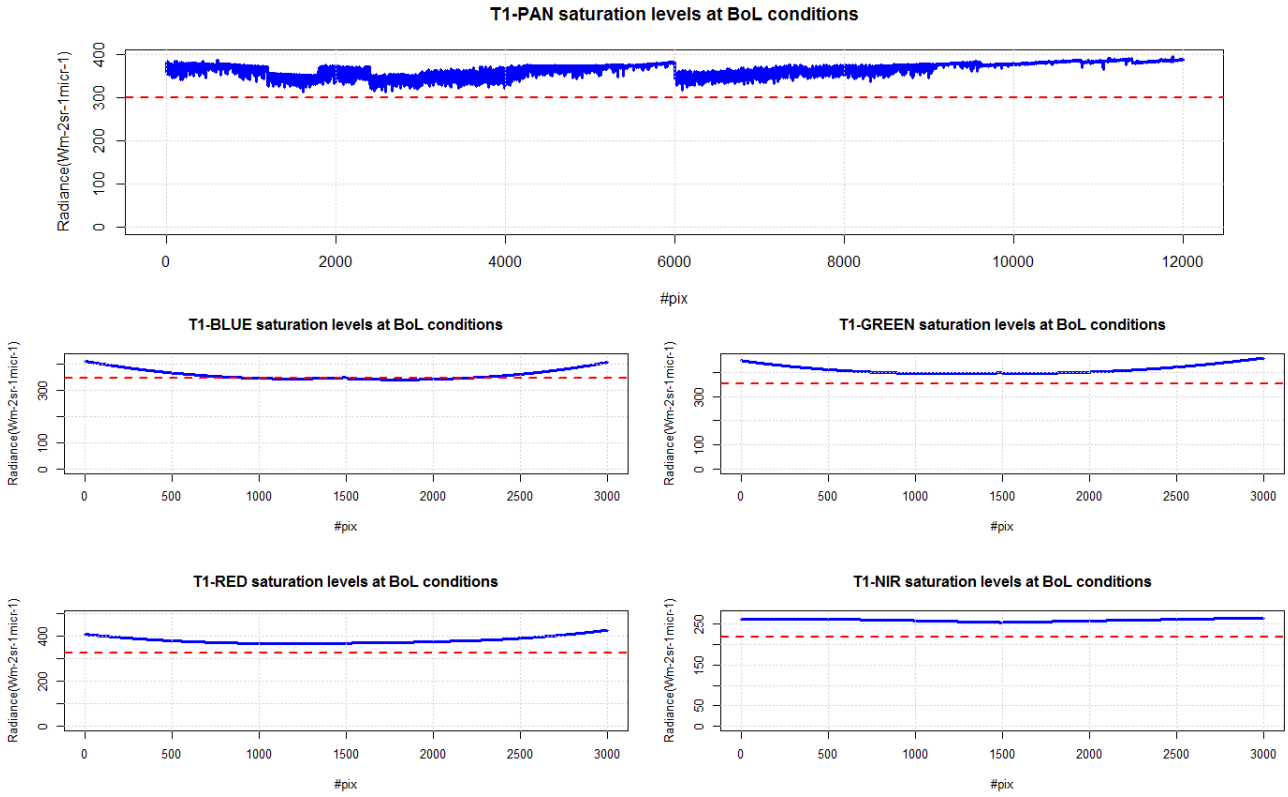

Figure 8. Saturation levels at BoL conditions for the PAN and four MS spectral channels.

Finally, in table 4 are presented the measured SNR values for T_1 and T_2 cameras, at the specified reference (L_{ref}) and minimum (L_{min}) radiances. For reference, it has been included in the table the SNR requirements at BoL conditions, for all channels and radiances. Albeit BoL SNR values have not been estimated from measurements yet, it is evident the large existing margin to requirement fulfillment, ranging from around a 30% up to a 100%, depending on the spectral channel and radiance level considered. These SNR ratios, together with the measured MTF values, ensure the excellent performance of the developed instrument.

Table 4. Measured SNR for PAN and MS channels of T_1 and T_2 telescopes, compared to BoL SNR requirements.

Channel	L_{ref} T_1	L_{ref} T_2	Rq. L_{ref}	L_{min} T_1	L_{min} T_2	Rq. L_{min}
PAN	153	152	110	75	73	50
MS-blue	242	234	125	167	159	85
MS-green	261	255	200	135	131	100
MS-red	258	266	200	104	109	80
MS-NIR	410	416	200	61	63	30

REFERENCES

[1] Miravet C., Zorita D., Santos C., Sánchez J. et al, "Correlation of INGENIO/SEOSAT radiometric model with the results of the radiometric campaigns", Proc. SPIE 10562, International Conference on Space Optics — ICSO 2016, (2017).
[2] Taubmann, G., Arroyo J.M., Miravet C., Zorita D. et al, "Finite element model assisted shimming of INGENIO/SEOSAT primary mirrors", Proc. SPIE 10562, International Conference on Space Optics — ICSO 2016, (2017).
[3] Marini. A., Reina Barragan F.J., Crippa G., Harnisch B. et al, "SEOSAT/INGENIO - a Spanish high-spatial-resolution optical mission", Proc. SPIE 10563, International Conference on Space Optics — ICSO 2014, (2017).
[4] Miravet C., Zorita D., Bueno J.I., Pascual L. et al, "Development status of the telescope for the Ingenio/SEOSAT mission primary payload", Proc. SPIE 8167, Optical Design and Engineering IV, (2011).
[5] Pascual L., Bueno J.I., Zorita D., Miravet C. et al, "Detailed Optical Design of SEOSAT/Ingenio Spanish High Resolution Imaging Instrument", International Conference on Space Optics — ICSO 2012.
[6] Zorita D., Miravet C. and Bueno J.I., "Challenges and developed solutions for the principal payload of the SEOSAT/Ingenio mission", RAQRS III, Recent Advances in Quantitative Remote Sensing, (2010).
[7] Markley F.L., "Attitude determination using vector observations and the singular value decomposition", Journal of the Astronautical Sciences, 38, 245-258 (1988).
[8] Efron B. and Tibshirani R., "Bootstrap methods for standard errors, confidence intervals, and other measures of statistical accuracy", Statistical Science, 1(1), 54-77 (1986).